Grant Agreement Period 4, Goal No. 2a (GAPG2a, Deliverable 5.5 of the MoU, COST Action CA15211

eLECTRONET

Satellite product development for atmospheric electricity

Co-ordinated by Konstantinos Kourtidis (GR) and Yaroslav Vyklyuk (UKR) with input from the CA15211 team

Abstract

There is no way to measure directly the near-ground electric field (potential gradient, PG) from space. We examine here the possibilities for deriving PG from space-borne observations as a higher-level product. Further, we present an approach to derive PG as well as tropospheric conductivity profiles and columnar resistance from space by combining satellite products with reanalysis data and a Long Short-Term Memory (LSTM) recurrent neural network model for deep learning.

Data and methods

Ground level data

We use mean daily data measured in the GLOCAEM station of Xanthi at 41.15°N, 24.92°E (Nicoll et al., 2019) during 2011-2018. More details on the measuring site and the instrumentation can be found at Kastelis and Kourtidis (2016). Potential gradient as well as meteorological variables (pressure, temperature, humidity, precipitation, wind speed and direction) measured at ground level (2 m height) are used. PG was measured with a Campbell CS110 field mill with a 1 sec resolution. Wind speed and direction were measured with a Wind Sentry Set (Model 03002L, Young Co., U.S.A) consisting of a 3-cup anemometer and a wind vane with accuracy +/-0.5 m s-1 and +/-5o, respectively. Temperature and relative humidity were measured with a thermometer/hygrometer of +/-1.5% and +/-0.3K accuracy (Model HygroClip S3, Rotronic Co., Switzerland). Pressure was measured with a barometric pressure sensor of 0.3 hPa accuracy (Model PTB110, Vaisala Co., Finland). Precipitation was measured with a tipping bucket rain gauge (Model 52202, Young Co., U.S.A.). The Fair-Weather PG (FWPG) mean daily values used here are the ones where hourly mean FWPG was available for >=12 hours.

Satellite data

We use MODIS/Aqua collections 5.1 and 6.1 data on aerosol optical depth (AOD), water vapor (WV), cloud cover fraction (CC), cloud optical depth (COD), cloud top pressure (CTP) and liquid water path (LWP).

Although not used here, since their potential application in the studied context is mentioned, a brief description of CALIOP data is presented: Since 2006, the Cloud-Aerosol Lidar with Orthogonal Polarization

(CALIOP), onboard the CALIPSO (Cloud-Aerosol Lidar and Infrared Pathfinder Satellite Observations) satellite, provides aerosol and cloud vertical profiles at global scale. CALIPSO is a sun-synchronous polar orbit satellite with an equatorial crossing time around 13:30 LT and approximately 16 days repetition orbit. CALIOP data are organized into different levels providing measured and retrieved quantities as well as higher-level products. At Level 1 (L1), fine resolution profiles of the attenuated backscatter at 532 and 1064 nm along with polarized backscatter in the visible channel are provided (Winker et al., 2009). The horizontal resolution of CALIOP L1 data is about one-third of a kilometer while in vertical terms varies from 30 to 180 m and from 60 to 180 m at 532 and 1064 nm, respectively, decreasing towards higher altitudes. After calibration and range correction, cloud and aerosol layers are identified and aerosol backscatter and extinction at 532 and 1064 nm are retrieved as part of the Level 2 (L2) dataset. For each category of detectable features (i.e. aerosols and clouds), subtyping algorithms are applied for the further discrimination in specific types (Omar et al., 2009). More specifically, in the latest available version (Version 4), the aerosol subcategories are: (i) marine, (ii) dust, (iii) polluted continental/smoke, (iv) clean continental, (v) polluted dust, (vi) elevated smoke, (vii) dust marine, (viii) PSC, (ix) volcanic ash and (x) sulfate. In CALIOP L2 data, the linear particle depolarization ratio at 532 nm (Winker et al., 2009) is also provided, which is a necessary parameter for the discrimination between spherical and non-spherical (e.g., dust) suspended particles. L2 products are delivered at 5 km horizontal resolution while in the vertical varies from 60 to 120 m, depending on the altitude range. Finally, the raw L2 products are aggregated to a gridded monthly mean Level 3 (L3) product, providing mean profiles of extinction at 532 nm and mean AOD at a 2° x 5° spatial grid resolution (Winker et al., 2013). Similar products, but at finer spatial resolution (1° x 1°), are available via the LIVAS (LIdar climatology of Vertical Aerosol Structure for space-based lidar simulation studies; lidar.space.noa.gr:8080/livas/; Amiridis et al., 2015) database. Major advancements have been applied in LIVAS, with respect to the raw CALIOP L3 data, including averaging calculation within the grid cell, a series of quality assurance filters (Marinou et al., 2017), a more realistic lidar ratio for Saharan dust (Amiridis et al., 2013) and the implementation of the depolarization-based separation method introduced by Tesche et al. (2009) for “isolating” dust component from aerosol mixtures.

Models

Data was joined to one DataFrame that consists time series of all input parameters and target field before future analysis :

$$\mathrm{DF} = (Key = t\colon Data =< \widetilde{In}_1(t), \dots, \widetilde{In}_n(t), \tilde{T}(t) >) \quad (1)$$

where t is date and time of the key field, $\widetilde{In}$ and $\tilde{T}$ are normalized input and output fields, respectively, *n* – number of input fields

A lag analysis was performed to determine the time delays between input and output factor. According to it, the time series of the input field was shifted by the investigated lag down and the correlation coefficient between it and the output fields was calculated. The results of the analysis are shown in Table 1.

Lag	WindSpeed (In_1)	WindDir (In_2)	T (In_3)	RH (In_4)	P (In_5)	Precipitation (In_6)	DewPoint (In_7)	AbsHumidity (In_8)	SpecificHumidity (In_9)	AOD (In_{10})	CC (In_{11})	WV (In_{12})	CTP (In_{13})	COD (In_{14})	LWP (In_{15})
0	0,11	0,22	-0,46	0,07	0,15	0,03	-0,51	-0,47	-0,52	-0,26	0,13	-0,40	0,01	-0,03	-0,05
1	0,10	0,20	-0,46	0,15	0,11	0,10	-0,45	-0,42	-0,45	-0,20	0,21	-0,37	-0,07	0,07	0,08
2	0,05	0,15	-0,45	0,19	0,09	0,10	-0,41	-0,37	-0,41	-0,18	0,25	-0,34	-0,11	0,11	0,11

3	0,02	0,13	-0,44	0,22	0,08	0,09	-0,38	-0,35	-0,38	-0,19	0,25	-0,34	-0,12	0,12	0,14
4	0,01	0,11	-0,43	0,22	0,07	0,09	-0,37	-0,34	-0,37	-0,21	0,23	-0,34	-0,10	0,10	0,12
5	0,00	0,10	-0,43	0,22	0,07	0,10	-0,36	-0,33	-0,37	-0,22	0,21	-0,34	-0,09	0,07	0,08
6	0,01	0,11	-0,42	0,22	0,06	0,07	-0,36	-0,33	-0,36	-0,22	0,20	-0,34	-0,08	0,08	0,08
7	0,00	0,10	-0,42	0,22	0,06	0,06	-0,36	-0,32	-0,36	-0,22	0,19	-0,34	-0,08	0,06	0,06
8	-0,01	0,08	-0,42	0,22	0,07	0,05	-0,35	-0,32	-0,36	-0,23	0,17	-0,34	-0,06	0,04	0,05
9	-0,02	0,05	-0,42	0,22	0,08	0,06	-0,36	-0,32	-0,36	-0,24	0,15	-0,34	-0,05	0,01	0,05
10	-0,01	0,06	-0,42	0,22	0,09	0,06	-0,36	-0,33	-0,36	-0,24	0,14	-0,33	-0,05	0,02	0,06

As can bee seen from the table there are not observed any linear and any lag dependencies (R<0.5 for all cases). The maximum of correlation coefficients is for lag 0 and 2. Therefore we will use in calculations data with this lag interval.

The Linear, back propagation neural networks (ANN) and a Long Short-Term Memory recurrent neural network (LSTM) model was used for deep learning.

The classical linear models, whose coefficients were calculated by regression analysis, were used as base models.

For using this type of models, the DataFrame (*DF*) must first be transformed into a shape:

$$\widetilde{DF} = (Key = t: Data =< \tilde{T}_1(t), \widetilde{In}_1(t), \dots, \widetilde{In}_n(t), \widetilde{In}_1(t-t_1), \dots, \widetilde{In}_n(t-t_1), \widetilde{In}_1(t-t_2), \dots, \widetilde{In}_n(t-t_2) >) \quad (2)$$

where *t* is date and time of the key field, $\widetilde{In}$ and $\tilde{T}$ are normalized input and output fields, respectively, and t_i - time lag.

The next step is to split $\widetilde{DF}$ into input and output data:

$$\widetilde{DF}_{tar} = (Key = t: Data_{tar} =< \tilde{T}_1(t) >) \quad (3)$$

$$\widetilde{DF}_{in} = (Key = t: Data_{in} = < \widetilde{In}_1(t), \dots, \widetilde{In}_n(t), \widetilde{In}_1(t-t_1), \dots, \widetilde{In}_n(t-t_1), \widetilde{In}_1(t-t_2), \dots, \widetilde{In}_n(t-t_2) >) \quad (4)$$

For LSTM model the tuple of the input field values ($Data_{in}$) was transformed into a three-dimensional form:

$$\widetilde{DF}_{LSTM,in} = (Key = t: Data_{in}^{3D} = \{d_{t,l,f}\}_{t=\overline{1,r_s},l=\overline{0,2},f=\overline{1,n}} >) \quad (5)$$

where d is input field of tuple $Data_{in}$, and indexes, t is time (number of rows), l is lag, f is input fields, r_s is number of rows of $\widetilde{DF}_{LSTM,in}$.

In order to improve the results, 2 types of neural networks were tested: Back propagation neural networks (ANN) and LSTM. This is a multilayered neural network, the algorithm of learning which method of reverse error propagation is chosen. This is one of the basic simple types of neural networks used in nonlinear dependency search tasks. In our calculation we used 2 layers ANN that consisted 10 neurons in each of the layers. The Adam Optimization Algorithm for Deep Learning was chosen for fitting. The DataFrames of input ($\widetilde{DF}_{in}$ *or* $\widetilde{DF}_{\mathrm{LSTM},in}$) and output $\widetilde{DF}_{tar}$fields was divided on training and test samples in proportion 70/30. The Tensorflow framework was chosen to implement this neural network.

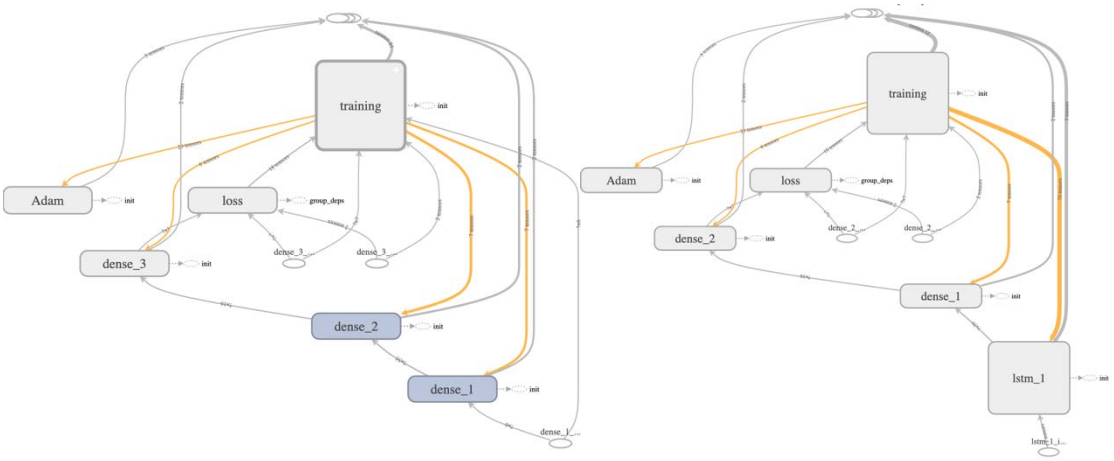

Figure 1. *Graph of ANN and LSTM neural networks.*

The structure of the network graph is presented in Figure 1.

This neural network allows you to simulate the behavior of a system that depends on time delay. This is realized by reverse transmission of the neural network output signal at the time t-1 back to the input of one of the network layers. This complex input is used to calculate the output for time t. LSTM is a type of the recurrent neural network, that allows memorizing values for long or short periods. This network does not use activation functions within its recurrent components. Thus, the stored value does not disappear iteratively over time. The LSTM blocks contain three or four "valves" that they use to control the information flow to or from their memory. These valves are used as logistic function to calculate values between 0 and 1. This value multiplies the allowance or denial a partial flow of information to or from that memory (Greff et al., 2017). In our calculations the LSTM consists 2 layers: first the LSTM with recurrent loops, and second the classical backpropagation layer (figure 1).

Requirements for a satellite product for atmospheric electricity: The case for PG

There is no way to measure directly the near-ground electric field (potential gradient, PG) from space. However, we develop here an approach to derive PG from space as a Level 4 product, i.e. by combining model results with analyses of lower-level data that are measured from space. We will examine below the

possibilities for deriving Fair-Weather PG (FWPG) from satellite data based on current satellite capabilities and possible future developments.

What would one need as input variables to derive FWPG? Are the input variables available as satellite products directly or can be modelled indirectly?

Firstly, we look at the variables that have been shown theoretically and/or experimentally to influence PG.

Water in the atmosphere can influence PG. Ground level Specific humidity is strongly anticorrelated with FWPG with an r^2 of -0.52 (see below). Columnar Water vapour (WV, from the MODIS/Aqua v5.1 collection) has been shown to excert a low influence on FWPG (r2=-0.03), with lower FWPG values for high water vapor amounts (Kourtidis and Georgoulias, 2017, see Fig. 2 below).

Stratiform **clouds** with low base height has been shown to influence surface PG, with lower PG values for lower cloud base height, due to negative charge of the cloud base (Nicoll and Harrison, 2016; Harrison et al., 2017). Cloud optical depth (COD, from the MODIS/Aqua v5.1 collection) has been shown to excerpt a moderate influence on FWPG (r2=-0.07), with lower FWPG values for high cloud optical depth (Kourtidis and Georgoulias, 2017, see Fig. 2 below). Based also on the results of Harrison et al., 2017, it seems that using not only MODIS COD but also MODIS cloud top height (CTH) or cloud top pressure (CTP) better correlations with FWPG could be found.

Atmospheric **aerosols** can influence ground level PG. In case of Saharan dust aerosols, the aerosol plume base is negatively charged through triboelectrification (Silva et al., 2016; Harrison et al., 2018), and hence diminishing PG, although different polarities may result from differences in the dust composition (Katz et al., 2018 and references therein). Fire smoke aerosols exert the opposite influence, considerably enhancing PG (Conceição et al., 2016), as do also anthropogenic aerosols, although to a lesser extend (Silva et al., 2014). Volcanic ash aerosols are also expected to exert an influence on PG (Aplin et al., 2016). Anthopogenic aerosol optical depth (AAOD, from the MODIS/Aqua v5.1 collection) has been shown to excerpt a moderate influence on FWPG (r2=-0.06), with lower FWPG values for high AAOD (Kourtidis and Georgoulias, 2017, see Fig. 2 below). Dust aerosol optical depth (DAOD, from the MODIS/Aqua v5.1 collection) has been shown to excerpt a somewhat stronger influence on FWPG (r2=-0.12), with lower FWPG values for high DAOD (Kourtidis and Georgoulias, 2017, see Fig. 2 below).

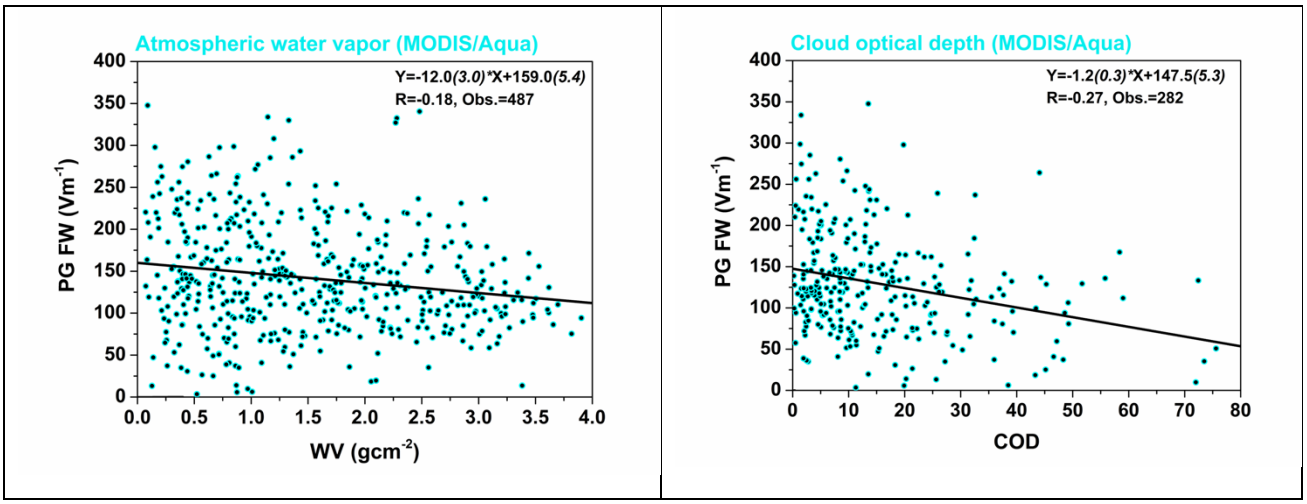

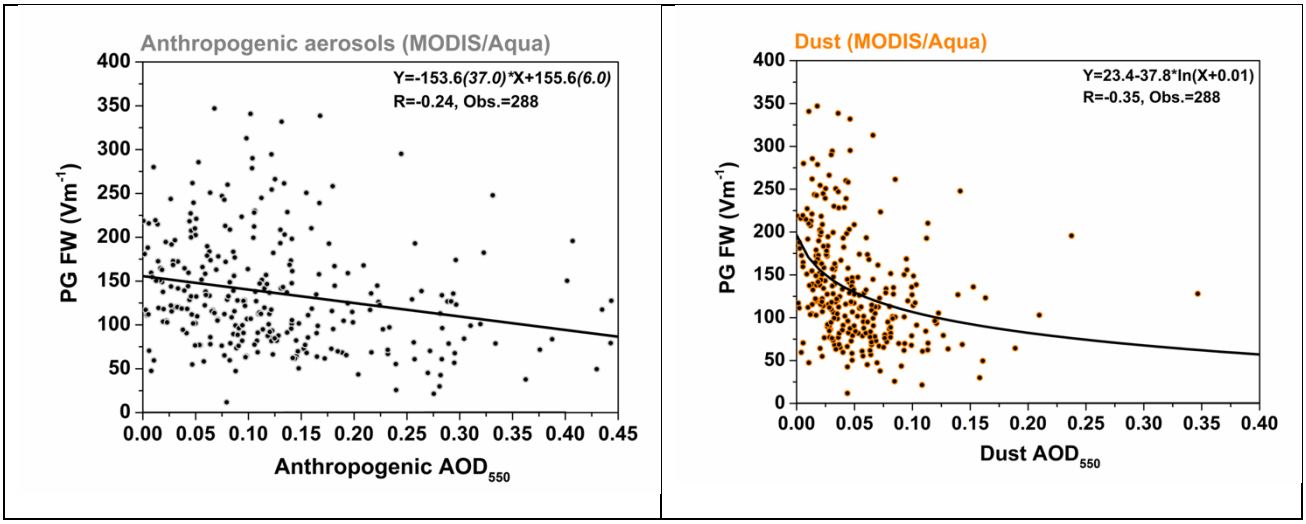

Figure 2. *Correlation between FWPG and the MODIS/Aqua satellite products (collection 5.1) of atmospheric water vapor, cloud optical depth, anthropogenic aerosols and dust aerosols (from* Kourtidis and Georgoulias, 2017*).*

So, it appears that the following columnar satellite products will be useful in deriving a PG level 4 product: Columnar Water vapour (WV), Cloud Optical Depth (COD), Cloud Top Pressure (CTP), Anthropogenic aerosols (AAOD), Dust (DAOD). They are available as satellite products from a variety of sensors, e.g. MODIS collection 6.1. As MODIS data are easily accessible as daily data, we will try to use mean daily PG data for our purposes.

Regarding both the cloud as well as the aerosol satellite data, improvements can be further achieved by using height-resolved satellite data. The only sensor currently capable of providing such data is the CALIOP Lidar onboard CALIPSO (Cloud-Aerosol Lidar and Infrared Pathfinder Satellite Observation), although the revisit time of 16 days limits its applicability.

To obtain FWPG from satellite data, we need to derive a function first, of the form FWPG=*f*(WV, COD, CTP, AOD, Wind Vel., T, humidity…..), or a model.

After some experiments with data analysis, we opt for an LSTM (Long Short-Term Memory, it is a Recurrent Neural Network architecture for deep learning) model FWPG trained with WV, CC, COD, LWP, AOD, Wind speed and direction, T, humidity, P and precipitation that appears to describe FWPG satisfactorily.

An LSTM Model of FWPG

At Table 1 the r^2 of the correlation between FWPG, AWPG and meteorological variables measured concurrently at ground level is shown while Table 2 shows the r^2 of the correlation between FWPG, AWPG and satellite-derived quantities.

Table 1. *Correlation (r2) between FWPG, AWPG and meteorological variables measured at ground level. AWPG and FWPG are in V/m. WS is the wind speed in m/s, WD is the wind direction in degrees, Prec is precipitation in mm, DewP is the dew point in ^{O}C, AbsH is absolute humidity in g/m3 and SpecH is specific humidity.*

	AWPG	FWPG	WS	WD	T(C)	RH(%)	P(hPa)	Prec	DP	AbsH	SpecH
AWPG	1	0,277	0,0855	0,077	-0,13	-0,07	0,14	-0,253	-0,211	-0,182	-0,238
FWPG	0,27	1	0,1142	0,216	-0,46	0,0667	0,149	0,0323	-0,509	-0,473	-0,516

WS	0,08	0,114	1	0,525	0,02	-0,27	-0,05	0,0986	-0,152	-0,138	-0,176
WD	0,07	0,216	0,5256	1	-0,16	-0,14	0,1317	0,0844	-0,303	-0,312	-0,283
T(C)	-0,139	-0,461	0,0201	-0,169	1	-0,546	-0,405	-0,086	0,8160	0,7852	0,771
RH(%)	-0,069	0,0667	-0,273	-0,143	-0,546	1	-0,044	0,2645	0,0273	0,0361	0,071
P(hPa)	0,144	0,1494	0,0565	0,1317	-0,405	-0,044	1	0,1866	0,5186	0,5080	-0,504
Prec	-0,254	0,0323	0,0986	0,0844	-0,086	0,264	-0,187	1	0,0671	0,0728	0,070
DewP	-0,211	-0,51	-0,152	-0,303	0,8160	0,0273	-0,519	0,0671	1	0,9752	0,972
AbsH	-0,182	-0,473	-0,138	-0,312	0,7852	0,0361	-0,508	0,0728	0,9752	1	0,899
SpecH	-0,238	-0,516	-0,176	-0,284	0,7717	0,0716	-0,504	0,0703	0,9720	0,8992	1

High anticorrelation is noted between FWPG with T (r2=0.46), Dew Point (r2=0.51) and specific humidity (r2=0.52). T can be obtained from reanalysis data e.g. from ERA-Interim or ERA5 (Dee at al., 2011), and specific humidity can be calculated from those reanalysis data of T, RH, P. ERA5 is produced using European Centre for Medium-Range Weather Forecasts' (ECMWF) Integrated Forecast System (IFS). Atmospheric data are interpolated to 37 pressure, 16 potential temperature and 1 potential vorticity level(s), with the top level at 0.01 hPa. "Surface or single level" data are also available, containing 2D parameters such as precipitation, 2m temperature, top of atmosphere radiation and vertical integrals over the entire atmosphere. (https://www.ecmwf.int/en/forecasts/datasets/archive-datasets).

ERA5 has much higher spatial resolution (31 km horizontal grid square instead of 79km for ERA-Interim), higher temporal information on variation in quality over space and time (1 hourly resolution instead of 6 hourly), much improved troposphere, better global balance of precipitation and evaporation, and more measurement parameters than ERA-Interim and can be downloaded from ECMWF.

From the satellite data of MODIS, high anticorrelation is noted between FWPG with WV (r2=0.40) and between FWPG and AOD (r2=0.26), whereas correlation between AWPG and the satellite -derived quantities is generally poor.

Table 2. *Correlation (r2) between FWPG, AWPG and satellite-derived quantities. AWPG and FWPG are in V/m. AOD is the aerosol optical depth, CC is the cloud cover fraction, WV is the column water vapour in cm, CTP is the cloud top pressure in hPa, COD is the cloud optical depth and LWP is the liquid water path in g/m2.*

	AWPG	**FWPG**	**AOD**	**CC**	**WV**	**CTP**	**COD**	**LWP**
AWPG	1	0,277	-0,01211	0,003602	-0,14646	0,051299	0,003991	-0,01388
FWPG	0,27	1	-0,26435	0,128304	-0,39712	0,012314	-0,03312	-0,04647
AOD	-0,01211	-0,26435	1	0,161416	0,361467	-0,15515	0,124979	0,127511
CC	0,003602	0,128304	0,161416	1	-0,03692	-0,77121	0,281205	0,409708

WV	-0,14646	-0,39712	0,361467	-0,03692	1	-0,16219	0,117814	0,09424
CTP	0,051299	0,012314	-0,15515	-0,77121	-0,16219	1	-0,14449	-0,3594
COD	0,003991	-0,03312	0,124979	0,281205	0,117814	-0,14449	1	0,738223
LWP	-0,01388	-0,04647	0,127511	0,409708	0,09424	-0,3594	0,738223	1

Training the models (LINEAR=Linear Model, LSTM=Long Short-Term Memory [Reccurent NN architecture for deep learning] and ANN=Artificial Neural Network) we obtain the results below when trying to reproduce measured FWPG from the models. LSTM performs better (Fig. 3). In Fig. 4 are the results for a portion of the timeseries, for clarity.

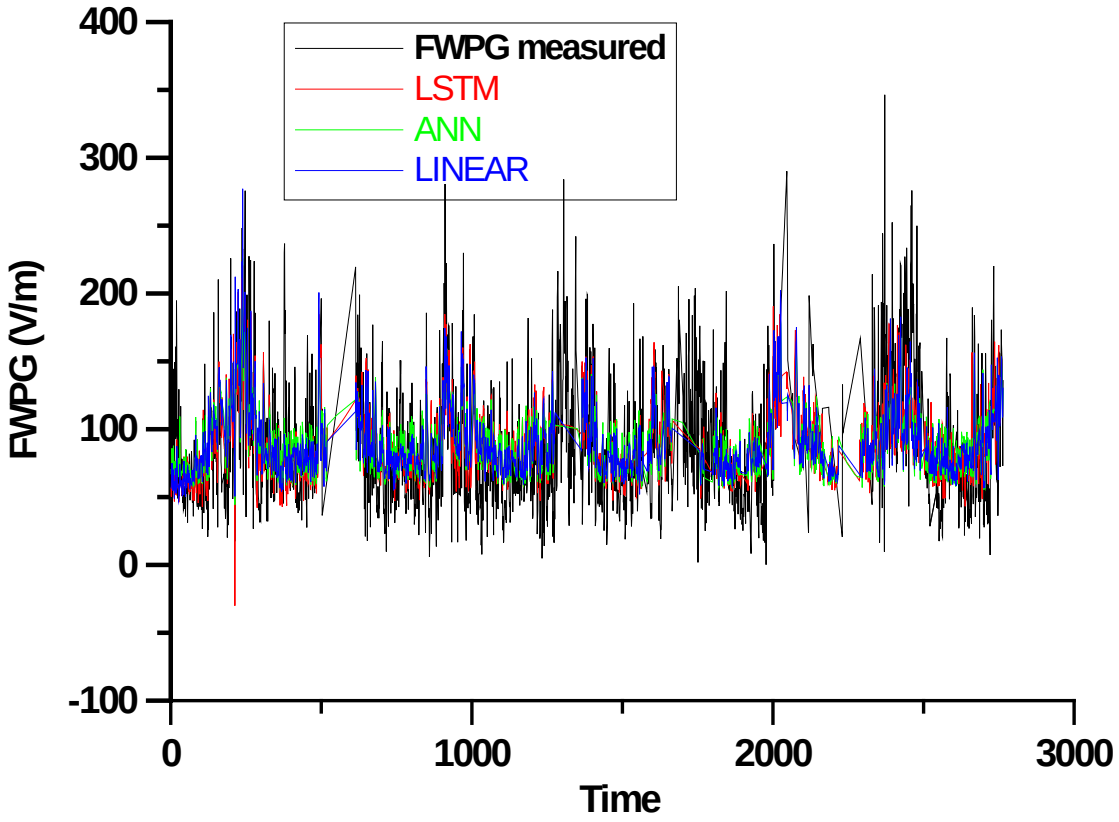

Figure 3. *Measured daily mean FWPG (only days where at least 12 hourly measurements are available) versus FWPG calculated with linear, ANN and LSTM models trained using wind speed, wind direction, temperature, relative humidity, pressure, precipitation, and specific humidity as input.*

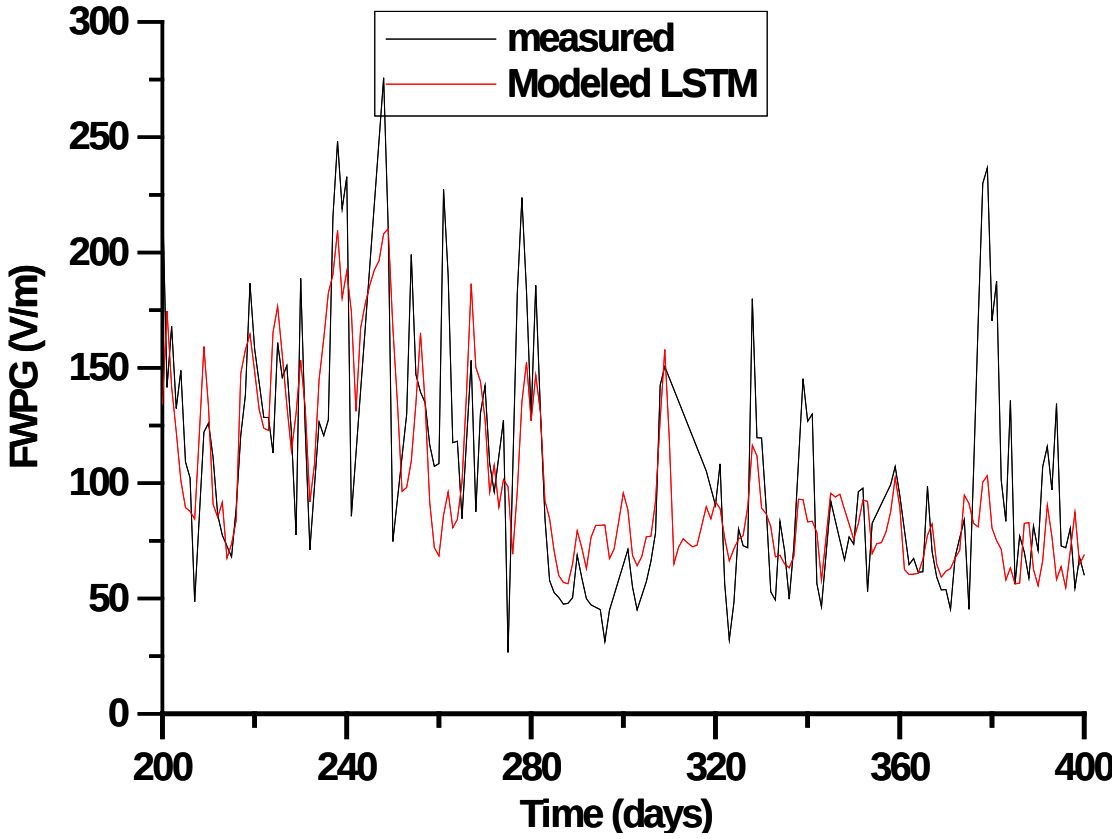

Figure 4. *Measured daily mean FWPG (only days where at least 12 hourly measurements are available) versus FWPG calculated with LSTM model, for a portion (200 days) of the timeseries.*

As, the LSTM model having as input the satellite derived quantities of AOD, CC, COD, CTP and WV and the temperature, Dew Point and specific humidity data which can be obtained from ERA5 can reproduce fairly well the variations of mean daily near-ground FWPG, it appears that in principle the derivation of a Level 4 product for FWPG is possible.

The wider spatial applicability of the model functions derived from a single site has to be studied.

Potential for further developments

1.A satellite product for conductivity profile and columnar resistance

A related physically-based approach could be considered vertically too, to allow calculation of the conductivity, either columnar or at various levels, and then integrated to obtain the columnar resistance. The optical depth data (either columnar from MODIS or vertical profiles from CALIOP) would give the aerosol term, and the cosmic ray ion production profile could come from relevant models, e.g. the CRAC-CRII (Usoskin and Kovaltsov, 2006; Usoskin et al., 2010) model.

Radon profiles would ideally be needed too for the lower atmosphere. ^{222}Rn has a half-life of 3.8 days and can produce ionization rates of 5–10 cm-3s-1 (Hoppel et al., 1986) near ground level, depending on convection. The vertical height distribution depends on convection, and is strongest in local summer, increasing the ^{222}Rn mixing ratio at higher altitudes, and decreasing the concentration at the surface, when compared to winter values. Other effects are due to advection by winds. The data of Dentener et al. (1999) for 222Rn concentrations in July and December near the surface, and estimates of the vertical distribution (Figure 2 of Dentener et al., 1999). The Dentener et al. [1999] data are in mBq SCM^{-1} (milli-Bequerel per standard cubic meter) obtained from the application of a global circulation model to the recommended World Climate Research Programme (WCRP) gaseous emission rate of ^{222}Rn.

As a Level 4 satellite product, conductivity and columnar resistance globally could be very useful. It could also be used for model validation, e.g. the validation of the CCM SOCOL v2 (Lucas, 2010; Mareev and Volodin, 2014). If the ionospheric potential was known (from one global measurement), it would allow the calculation of the global circuit component of the surface potential gradient. As 90% of the atmospheric columnar resistance is below 6-7 km altitude (Rycroft et al., 2008), and as satellite products of tropospheric profiles of aerosols and clouds are available from CALIOP, conductivity profiles could be derived, as explained further below.

As column resistance is defined as the vertical integration of the reciprocal of conductivity,

$$R_{col} = \text{surface to ionosphere} \int 1 dz/\sigma(z) ,$$

where dz are the layer thicknesses, then the column resistance could also be calculated from satellite data.

Given the fact that most of the resistance is in the troposphere, and that the CALIOP vertical resolution varies from 60 to 120 m at 532 nm, decreasing towards higher altitudes, a dz varying around 500 m to fit the CALIOP layers could be used.

A close correlation exists between the concentration of small ions and polar conductivity near the surface of Earth. In the presence of large aerosol particles, losses in the small ion concentration are caused not only due to the ion–ion recombination process, but also due to attachment of small ions to the aerosol particles. This renders the small ions almost immobile and causes a decrease in conductivity of the atmosphere. This results in an expected inverse relationship between the aerosol concentration and the electrical conductivity (Cobb and Wells, 1970; Cobb, 1973). Mani and Huddar (1972) observed a decrease in conductivity presumably caused by the increase in particles at Pune, India over a period of 20 years and Kamra and Deshpande (1995) attributed the increase of conductivity over the Bay of Bengal with distance from the coast to land air pollution outflow. Hogan et al., (1973) pointed out that the conductivity inversely follows the product of aerosol size and number density better than the number density alone. Retalis (1977) noted the negative correlation between smoke and small air ions concentration in Athens.

Since aerosols influence not only the small air ion concentration but also the optical properties of the atmosphere, a relationship between optical and electrical properties should be expected. Such a relationship is supported by observations. On hourly timescales, Ruhnke (1966) reported a positive correlation between visibility and ion number concentration, and Manes (1977) showed coincident decreasing annual trends in visibility and conductivity. Tsunoda and Satsutani (1977) found increases in visibility coincident with both an increase in air conductivity and particle number concentration decreases. Brazenor and Harrison (2005) also found an empirical relationship between air conductivity and visibility, for urban air.

Harrison (2012) derived theoretically aerosol–conductivity relationships for fog droplets and compared these with routine visual range and potential gradient measurements. The relationship between the electrical and optical properties of air can be understood in terms of common aerosol effects on both quantities, by combining the theoretical descriptions independently available in each case.

Using an approach similar to the modelling approach of Baumgartner et al (2014) but using satellite data instead and the Harrison (2012) parameterization one could obtain columnar resistance from satellite data.

2.Estimations of ionospheric potential

Lightning is a parameter that can be obtained from satellites to estimate the source regions of the GEC. By observing the global distribution of lightning, it is possible to locate the thunderstorm regions, and assign estimates of the conduction currents produced above these storms. The sum of all these currents (~1 Amp each storm) will supply the total current in the GEC. Knowing the resistance of the fair-weather portion of the atmosphere (see above) will allow us to estimate the ionospheric potential.

3. Other

The source region of the GEC is defined by both shower clouds and thunderstorms that produce conduction currents up to the ionosphere. One indicator of the intensity of thunderstorms is from the microwave emissions from the top of storm clouds. While the intensity of thunderstorms is not necessarily related to the current density above these storms, it does allow us to map out the location of the source generators. http://severeweather.wmo.int/TCFW/RAIV_Workshop2017/08a_Microwave_Lecture_JohnCangialosi_DaveRoberts.pdf

Conclusions

Acknowledgements

Based upon work from COST Action "Atmospheric Electricity Network: coupling with the Earth System, climate and biological systems (ELECTRONET)", supported by COST (European Cooperation in Science and Technology).

References

Amiridis, V., Wandinger, U., Marinou, E., Giannakaki, E., Tsekeri, A., Basart, S., Kazadzis, S., Gkikas, A., Taylor, M., Baldasano, J., and Ansmann, A.: Optimizing CALIPSO Saharan dust retrievals, Atmos. Chem. Phys., 13, 12089–12106, doi:10.5194/acp-13- 12089-2013, 2013.

Amiridis, V., Marinou, E., Tsekeri, A., Wandinger, U., Schwarz, A., Giannakaki, E., Mamouri, R., Kokkalis, P., Binietoglou, I., Solomos, S., Herekakis, T., Kazadzis, S., Gerasopoulos, E., Proestakis, E., Kottas, M., Balis, D., Papayannis, A., Kontoes, C., Kourtidis, K., Papagiannopoulos, N., Mona, L., Pappalardo, G., Le Rille, O., and Ansmann, A.: LIVAS: a 3-D multi-wavelength aerosol/cloud database based on CALIPSO and EARLINET, Atmos. Chem. Phys., 15, 7127–7153, doi:10.5194/acp-15-7127- 2015, 2015.

Aplin, K.L., Bennett, A.J., Harrison, R.G., Houghton, I.M.P., Electrostatics and In Situ Sampling of Volcanic Plumes, Chapter 6, Volcanic Ash: Hazard Observation pp. 99-113, 2016.

Baumgaertner A. J. G., G. M. Lucas, J. P. Thayer, and S. A.Mallios, On the role of clouds in the fair weather part of the global electric circuit, Atmos. Chem. Phys., 14, 8599–8610, doi:10.5194/acp-14-8599-2014, 2014.

Brazenor T.J., and R.G. Harrison, Aerosol modulation of the optical and electrical properties of urban air, Atmos. Env., 39, 28, 5205-5212, 2005.

Cobb, W.E., Oceanic aerosol levels deduced from measurements of the electrical conductivity of the atmosphere, Journal of Atmospheric Science, 30, 101-106, 1973.

Cobb, W.E. & Wells, H.J., The electrical conductivity of oceanic air and its correlation to global atmospheric pollution. Journal of Atmospheric Science, 27, 814-819, 1970.

Conceição, R., Melgão, M., Silva, H.G., (...), Harrison, R.G., Reis, A.H., Transport of the smoke plume from Chiado's fire in Lisbon (Portugal) sensed by atmospheric electric field measurements, Air Quality, Atmosphere and Health 9(3), pp. 275-283, 2016.

Dee, D. P., Uppala, S. M., Simmons, A. J., Berrisford, P., Poli, P., Kobayashi, et al., The ERA-Interim reanalysis: configuration and performance of the data assimilation system. Q.J.R. Meteorol. Soc., 137: 553–597. doi:10.1002/qj.828, 2011.

Dentener, F., J. Feichter, and A. Jueken, Simulation of the transport of Rn222 using on-line and off-line global models at different horizontal resolutions: A detailed comparison with measurements, Tellus, Ser. B, 51, 573–602, 1999.

Greff, K., Srivastava, R.K., Koutník, J., Steunebrink, B.R., Schmidhuber, J., IEEE Transactions on Neural Networks and Learning Systems 28(10):2222–2232. DOI 10.1109/TNNLS.2016.2582924, 2017.

Harrison, R.G., Aerosol-induced correlation between visibility and atmospheric electricity, Journal of Aerosol Science 52, 121–126, 2012.

Harrison, R.G., Nicoll, K.A., Aplin, K.L., Evaluating stratiform cloud base charge remotely, Geophysical Research Letters 44(12), 6407-6412, 2017.

Harrison, R.G., Nicoll, K.A., Marlton, G.J., Ryder, C.L., Bennett, A.J., Saharan dust plume charging observed over the UK, Environmental Research Letters 13(5),054018, 2018.

Hogan A.W., V.A. Mohnen, V.J. Schaefer, Comments on “Oceanic aerosol levels deduced from measurements of the electrical conductivity of the atmosphere”, J. Atmos. Sci., 30, 1455-1460, 1973.

Hoppel, W. A., R. V. Anderson, and J. C. Willett, Atmospheric electricity in the planetary boundary layer, in The Earth’s Electrical Environment, pp. 149–165, Natl. Acad. Press, Washington, D. C.1, 1986.

Kamra, A.K. and Deshpande, C.G., Possible secular change and land-to ocean extension of air pollution from measurements of electrical conductivity over the Bay of Bengal, J. Geophys. Res., 100, 7105–7110, 1995.

Kastelis N. and K. Kourtidis: Characterisation of the atmospheric electric field and correlation with CO2 at a rural site in southern Balkans, Earth, Planets and Space, 68:3, DOI 10.1186/s40623-016-0379-3, 2016.

Katz, S., Yair, Y., Price, C., (...), Lynn, B., Ziv, B., Electrical properties of the 8–12th September, 2015 massive dust outbreak over the Levant, Atmospheric Research 201, pp. 218-225, 2018.

Kourtidis K. and A. Georgoulias, Impact of aerosols, dust, water vapor and clouds on fair weather PG and implications for the Carnegie curve, EGU General Assembly 2017, Vienna 23-28 April 2017, Geophysical Research Abstracts Vol. 19, EGU2017-4815, 2017.

Lucas, G. M., Investigating the physical mechanisms that impact electric fields in the atmosphere. Thesis, B.S., University of Wisconsin, 2010.

Manes, A., Particulate air pollution deduced from atmospheric electrical conductivity measurements at Bet-Dagan (Israel). In: H. Dolezalek, & R. Reiter (Eds.), Electrical Processes in Atmospheres. Steinkopf Verlag, 109–118, 1977.

Mani, A. and Huddar, B.B., Studies of the surface aerosols and their effect on atmospheric electric parameters. Pure and Applied Geophysics, 100, 154–166, 1972.

Mareev, E. A., and E. M. Volodin, Variation of the global electric circuit and Ionospheric potential in a general circulation model, Geophys. Res. Lett., 41, 9009–9016, doi:10.1002/2014GL062352, 2014.

Marinou, E., Amiridis, V., Binietoglou, I., Tsikerdekis, A., Solomos, S., Proestakis, E., Konsta, D., Papagiannopoulos, N., Tsekeri, A., Vlastou, G., Zanis, P., Balis, D., Wandinger, U., and Ansmann, A.: Three-

dimensional evolution of Saharan dust transport towards Europe based on a 9-year EARLINET-optimized CALIPSO dataset, Atmos. Chem. Phys., 17, 5893–5919, https://doi.org/10.5194/acp-17-5893-2017, 2017.

Nicoll, K. A., and R. G. Harrison, Stratiform cloud electrification: Comparison of theory with multiple in-cloud measurements, *Q. J. R. Meteorol. Soc.*, 142(700), 2679– 2691, 2016.

Nicoll K.A., Harrison R G., V. Barta, J. Bor, R. Brugge, A. Chillingarian, J. Chum, A. K. Georgoulias, A. Guha, K. Kourtidis, M. Kubicki, E. Mareev, J. Matthews, H. Mkrtchyan, A. Odzimek, J.-P. Raulin, D. Robert, H. Silva, J. Tacza, Y. Yair, R. Yaniv, A global atmospheric electricity monitoring network for climate and geophysical research, Journal of Atmospheric and Solar-Terrestrial Physics, 184, 18-29, doi.org/10.1016/j.jastp.2019.01.003, 2019.

Omar, A., Winker, D., Kittaka, C., Vaughan, M., Liu, Z., Hu, Y. X., Trepte, C., Rogers, R., Ferrare, R., Lee, K., Kuehn, R., and Hostetler, C.: The CALIPSO automated aerosol classification and lidar ratio selection algorithm, J. Atmos. Ocean. Tech., 26, 1994–2014, doi:10.1175/2009jtecha1231.1, 2009.

Retalis D.A., On the relationship between small atmospheric ions concentration and (1) smoke, (2) sulfur dioxide and (3) wind speed, pure and applied geophysics 115, 3, 575–581, 1977.

Ruhnke, L.H., Visibility and small-ion density. Journal of Geophysical Research, 71, 4235–4241, 1966.

Rycroft M.J., R. Giles Harrison, Keri A. Nicoll, Evgeny A. Mareev, An Overview of Earth's Global Electric Circuit and Atmospheric Conductivity, Space Sci. Rev., DOI 10.1007/s11214-008-9368-6, 2008.

Silva, H.G., Conceição, R., Melgão, M., (...), Reis, A.H., Harrison, R.G., Atmospheric electric field measurements in urban environment and the pollutant aerosol weekly dependence, Environmental Research Letters 9(11),114025, 2014.

Silva, H.G., Lopes, F.M., Pereira, S., (...), Harrison, R.G., Collares Pereira, M., Saharan dust electrification perceived by a triangle of atmospheric electricity stations in Southern Portugal, Journal of Electrostatics 84, pp. 106-120, 2016.

Tesche, M., Ansmann, A., Müller, D., Althausen, D., Engelmann, R., Freudenthaler, V., and Grob, S.: Vertically Resolved Separation of Dust and Smoke over Cape Verde Using Multiwavelength Raman and Polarization Lidars during Saharan Mineral Dust Experiment 2008, J. Geophys. Res., 114, D13202, doi:10.1029/2009JD011862, 2009.

Tsunoda, Y., & Satsutani, T., Observation of atmospheric ions and atmospheric phenomena in the area of Kobe, Japan. In: H. Dolezalek, & R. Reiter (Eds.), Electrical Processes in Atmospheres. Steinkopf Verlag, pp. 135–142, 1977.

Usoskin, I. G., and G. A. Kovaltsov, Cosmic ray induced ionization in the atmosphere: Full modeling and practical applications, J. Geophys. Res., 111, D21206, doi:10.1029/2006JD007150, 2006.

Usoskin, I. G., G. A. Kovaltsov, and I. A. Mironova, Cosmic ray induced ionization model CRAC:CRII: An extension to the upper atmosphere, J. Geophys. Res., 115, D10302, 2010.

Winker, D. M., Vaughan, M. A., Omar, A. H., Hu, Y., Powell, K. A., Liu, Z., Hunt, W. H., and Young, S. A.: Overview of the CALIPSO Mission and CALIOP Data Processing Algorithms, J. Atmos. Ocean. Tech., 26, 2310–2323, doi:10.1175/2009JTECHA1281.1, 2009.

Winker, D. M., Tackett, J. L., Getzewich, B. J., Liu, Z., Vaughan, M. A., and Rogers, R. R.: The global 3-D distribution of tropospheric aerosols as characterized by CALIOP, Atmos. Chem. Phys., 13, 3345–3361, doi:10.5194/acp-13-3345-2013, 2013.